Carbon 171 (2021) 493–506

Contents lists available at ScienceDirect

Carbon

journal homepage: www.elsevier.com/locate/carbon

Research Article

Graphene quantum dots induced porous orientation of holey graphene nanosheets for improved electrocatalytic activity

Mumtaz Ali [a, 1], Rabia Riaz [a, 1], Aima Sameen Anjum [a], Kyung Chul Sun [a], Hui Li [b], Sung Hoon Jeong [a, *], Min Jae Ko [b, c, **]

[a] Department of Organic and Nano Engineering, Hanyang University, 222 Wangsimni-ro, Seongdong-gu, Seoul, 04763, Republic of Korea
[b] Department of Chemical Engineering, Hanyang University, 222 Wangsimni-ro, Seongdong-gu, Seoul, 04763, Republic of Korea
[c] Institute of Nano Science and Technology, Hanyang University, 222 Wangsimni-ro, Seongdong-gu, Seoul, 04763, Republic of Korea

ARTICLE INFO

Article history:
Received 8 August 2020
Received in revised form
10 September 2020
Accepted 12 September 2020
Available online 15 September 2020

Keywords:
Phase separation
Nitrogen doped graphene quantum dots
Antisolvent effect
Holey graphene oxide
Electrocatalysis
Counter-electrode

ABSTRACT

Complex electrolyte diffusion through the stacked graphene nanosheets limits their electrochemical performance. As a potential solution, this study explored the potential of nitrogen-doped graphene quantum dots (NGQDs) to induce 3D porous orientation of holey graphene oxide (hGO) nanosheets. The sizes of NGQDs and antisolvent for phase separation assisted assembly were optimized to achieve a 3D nanoporous network. This nano-network serves as a soft template for the porous orientation of hGO, forming a 3D hierarchically porous carbon architecture. Benefiting from the porosity of the 3D framework, π-π restacking was radically avoided, providing high electrolyte transport rates. In addition, doped nitrogen and J-type aggregation of NGQDs effectively tuned the band structure to realize charge transfer at low overpotential. The enhanced electrocatalytic activity and exceptionally low charge transfer resistance of the composite structure were attributed to the enhanced electrode/electrolyte interface and multidimensional charge & electrolyte transport. Porous composite structure based counter electrode showed 78% enhanced photovoltaic performance (compared to unmodified graphene) in the dye-sensitized solar cell, which is comparable to the performance of Pt electrode. The proposed 3D porous orientation can be utilized in emerging electrocatalytic applications, such as supercapacitors, water splitting, and battery electrodes.

1. Introduction

Stacked and nonporous structures of carbon materials limit their associated reaction rates due to the complex diffusion kinetics of electrolyte ions; thus, superior porosity and high exposed surface area are crucial parameters for unlocking the full potential of carbon materials [1]. Specifically, such sluggish kinetics are more severe in the case of 2D carbon nanosheets—reduced graphene oxide (rGO) [2]. The theoretical surface area and surface reactivity of rGO is ideal for electrochemical energy storage and electrocatalytic devices; however, π-π stacking poses a great obstacle in practical applications [3–6]. In order to overcome this problem, rGO sheets have been oriented with different macrostructures to directly manipulate the electrocatalytic activity by varying the macro-assembly of rGO nanosheets. For instance, graphene balls [7,8], crumpled graphene [9], graphene with spacer materials [10], vertically aligned graphene [11], and holey graphene oxide (hGO) [12–14] have been fabricated to increase the exposed surface area and electrolyte mobility. Such macro architectures alter the interfacial activity by weakening the interplanar forces responsible for the restacking of rGO sheets. In this regard, we propose a highly porous assembly of hGO sheets by utilizing the strong self-assembly behavior of nitrogen-doped graphene quantum dots (NGQD) inclusions.

NGQDs possess a chemical structure similar to that of rGO; however, due to their extremely small size, NGQDs can accommodate an exceptionally high amount of functional groups and edge surfaces [15]. In addition, the NGQDs synthesis process generates a byproduct holey graphene oxide (hGO), that can replace rGO sheets

* Corresponding author.
** Corresponding author. Department of Chemical Engineering, Hanyang University, 222 Wangsimni-ro, Seongdong-gu, Seoul, 04763, Republic of Korea.
E-mail addresses: shjeong@hanyang.ac.kr (S.H. Jeong), mjko@hanyang.ac.kr (M.J. Ko).
[1] M. Ali and R. Riaz contributed equally to this work.

https://doi.org/10.1016/j.carbon.2020.09.031
0008-6223/

[6,16]. The quantum size endows exciting features in NGQDs; hence, NGQDs inclusions are used to reinforce the thermal and electrical conductivity [17], capillary action [18], and flexibility of graphene fibers and films [19]. NGQDs are composed of a graphene-like planar structure formed by fused aromatic rings, separated by oxygenated/nitrogenated sp^3-hybridized carbons [20]. Along with the quantum size, the hybridization and oxidization of NGQDs impart an amphiphilic polymer like behavior. For example, the amphiphilic nature of NGQDs has recently been identified to orient them in nanowalls architecture by utilizing ethanol as an antisolvent [21]. In this case, phase separation occurs due to the difference in the solubility of NGQDs in water and ethanol, leading to rich phase (in water/solvent) and poor phase (in antisolvent/ethanol) NGQDs. The NGQD-rich phase has a high density of NGQDs, and the NGQD-poor phase has an almost negligible content of NGQDs [6]. Similarly, superior phase-separation assembly was observed using propanol, which results in a 3D porous structure. NGQDs assemblies were fabricated as an overlayer on rGO nano-sheets for the degradation of organic dyes [6]. Nevertheless, the incorporation of conductive nanosheets (rGO/hGO) is important for charge transport and electrocatalysis because pure NGQD films have limited conductivity. However, the phase separation effect of NGQDs is not sufficiently strong to orient rGO nanosheets or other nanomaterials; hence, a uniform film is formed if conductive nano-inclusions are incorporated into porous assemblies of NGQDs. The motivation for this work was to realize a strong phase separation effect in NGQDs by optimizing their size and antisolvent, which can serve as a soft template for the orientation of hGO nanosheets. Our proposed concept of orienting hGO nano-sheets (larger) using NGQDs (smaller) is inspired by ants, as they can lift loads heavier than their own size/weight.

In this study, we synthesized three different sizes of NGQDs, and their phase separation assisted porous assembly was optimized using N–N dimethylacetamide (DMA) as an antisolvent. Among all sizes, the smallest size (2–5 nm) of NGQDs showed the strongest phase separation and they self-assembled to form nanoflowers. This nano-framework serves as a soft substrate for the orientation of hGO nano-sheets, which are a byproduct of the NGQDs synthesis process. The remarkable surface functionality of NGQDs coupled with the efficient porous assembly provides an outstanding electrocatalytic activity in the proposed composite structure. The J-type aggregation and doped nitrogen from the smallest sized NGQDs effectively tuned the band structure to realize redox reaction at lower overpotential. In contrast, the orientation of the larger NGQDs was not sufficient to orient the hGO nano-sheets; hence, the reaction rate was limited by electrolyte diffusion in the stacked composite structure. The photovoltaic performance of the oriented composite structure of NGQDs and hGO was examined using a counter electrode in dye-sensitized solar cells (DSSCs). Compared to the rGO-based counter electrode, the oriented composite structure showed 78% enhanced photovoltaic performance. Overall, the performance of the optimized structure was similar to that of Pt electrodes, which are commonly used as a counter electrode for DSSCs.

2. Materials and method

2.1. Materials

Graphite powder with a size of less than 100 μm (Asbury, America) was used as a starting material for the synthesis of GO and NGQDs. Other chemicals used for the exfoliation and cutting of graphite, including sulfuric acid (99%), potassium permanganate ($KMnO_4$), hydrogen peroxide (H_2O_2, 30%), hydrochloric acid (HCl, 35%), and ammonium hydroxide (NH_4OH, 30%) were purchased from Sigma Aldrich. Purification and separation of different sizes were performed using dialysis membranes of 0.3 kDa, 1 kDa, 10 kDa, and 50 kDa, provided by Cellu Sep ®, USA. Other common solvents used in the experiment were purchased from Daejung chemicals, Ltd. The materials required for the fabrication of DSSC (TiO_2 paste, N719 dye, and ionomer Surlyn (60 μm)) were collected from Dyesol, Australia. F-doped tin oxide (FTO) glass with a surface resistance of 7 Ω/□ was purchased from Pilkington. Other chemicals required for solar cell fabrication ($TiCl_4$, electrolyte ingredients, and chloroplatinic acid) were purchased from Sigma Aldrich.

2.2. Synthesis of graphene oxide sheets

Graphite powder was exfoliated to synthesize GO using the modified hummers method as stated previously [10,21]. In brief, uniform dispersion of graphite (5 g) was achieved in pure sulfuric acid (150 ml) through vigorous magnetic stirring. The graphite dispersion was transferred to an ice bath to lower the temperature below 5 °C. Maintaining the temperature below 10 °C, $KMnO_4$ (25 g) was slowly added to the dispersion. The temperature of the dispersion was then retained at 35 °C for 8 h. Complete oxidation of graphite to graphite oxide can be identified by the change in color to dark brown. To stop the oxidation process, the temperature of the dispersion was further decreased to 5 °C by transferring it to an ice bath. Maintaining a low temperature, 500 ml of deionized water was added dropwise with continuous stirring. Finally, for the conversion of graphite oxide to GO sheets, which is indicated by the appearance of bright yellow color, 8–10 ml of H_2O_2 was added dropwise. The GO solution was subjected to washing by centrifugation with dilute HCl and acetone to remove metallic and organic impurities, respectively. The purified GO dispersion was further subjected to ultra-purification by dialyzing it against water using a cellulose membrane with a molecular weight cut-off of 50 kDa. The purified GO dispersion was finally dried using lyophilizer to obtain the GO powder.

2.3. Synthesis of NGQDs and hGO

One-step nitrogen doping and cutting of graphene oxide sheets were performed following the previously reported hydrothermal cutting of GO sheets [6,21]. In brief, a 0.2% solution (200 mL) of GO was prepared by sonication, followed by the addition of NH_4OH (20 mL) and H_2O_2 (10 mL). The mixture of the reactants was then transferred to a Teflon-lined titanium hydrothermal chamber for heating at 200 °C for 4 h. At high temperatures, the GO sheets are cut into small nitrogen-doped chunks of less than 20 nm size, known as NGQDs. Additionally, holey graphene sheets (hGO) are also formed, which can be separated by repeated centrifugation or filtration, as depicted schematically in Fig. 1. The cutting of GO sheets into smaller components is attributable to the etchant nature of H_2O_2 and NH_4OH [22]. To remove extra small organic impurities, the NGQD solution was dialyzed with the 0.3 kDa dialysis membrane. For the separation of different sizes of NGQDs, dialysis membranes of different sizes (1, 10, and 50 kDa) were used, as shown in Fig. 1. Samples were dialyzed with each type of membrane for 3 days; however, depending on the quantity of water used in the dialysis process, the time can be varied. The colloidal solution of NGQDs was concentrated using a rotary evaporator. The restacking of NGQDs is reversible (unlike rGO nanosheets); therefore, freeze-drying is not a compulsory concentration procedure for NGQDs. The separation is facilitated by the difference in the molecular weight cut-off of the membranes; therefore, the samples were named according to the size of the membrane used for separation. NGQDs separated by the 1 kDa, 10 kDa, and 50 kDa membranes were labeled as GD-1, GD-10, and GD-50, respectively (Fig. 1). Typical NGQDs mixture approximately contains 40%, 25%, and 35% of GD-1, GD-10, GD-50.

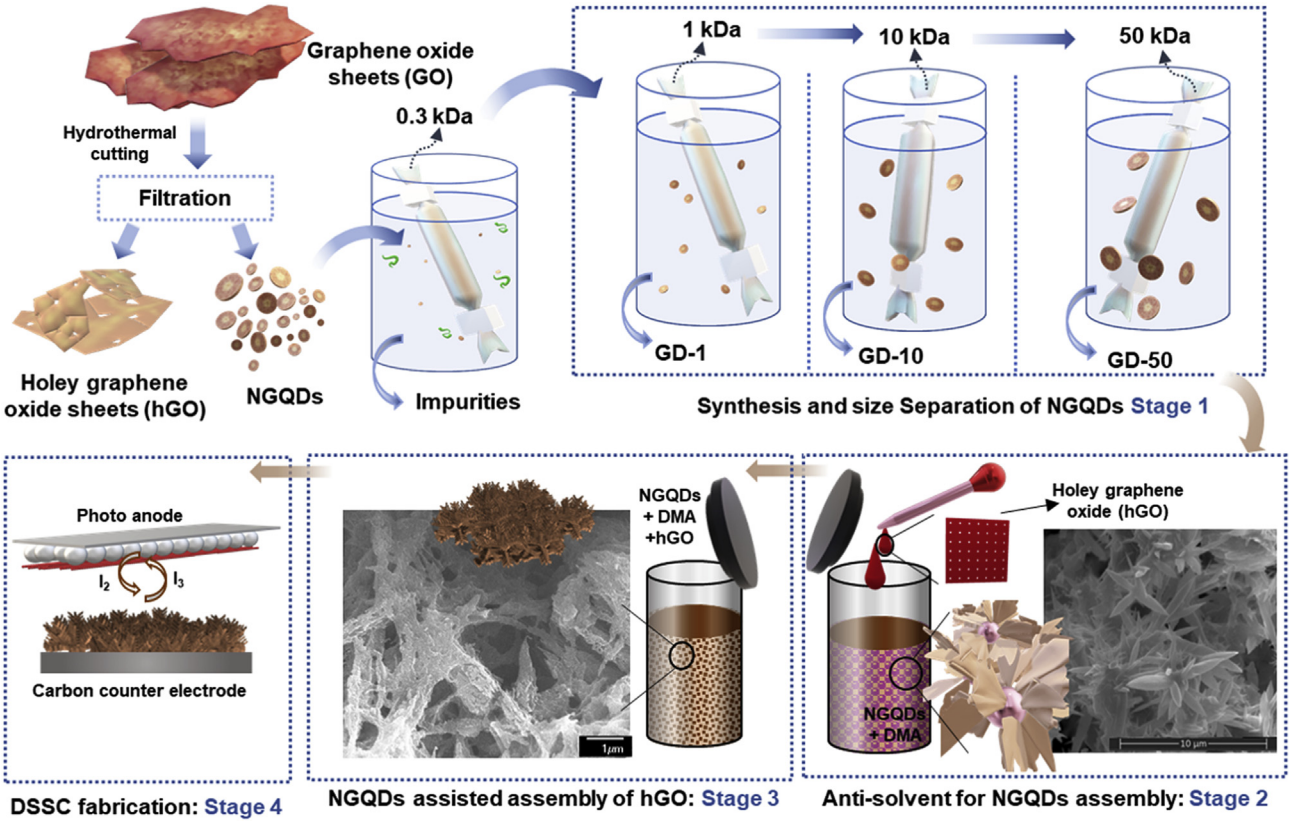

Fig. 1. Schematic illustration of experimental design. Initially, the different sizes of NGQDs were synthesized by hydrothermal cutting of GO sheets and separated by dialysis membranes. The phase separation behavior of different sizes of NGQDs was optimized to achieve porous support. NGQDs assisted oriented hGO sheets formed a porous network, which was used as a counter electrode for DSSC. (A colour version of this figure can be viewed online.)

2.4. DSSC fabrication

The previously optimized method of double main layer and single scattering layer was followed for the fabrication of the photoanode [23]. Starting with the deposition of the blocking layer on the photoanode, washed FTO glass was subjected to $TiCl_4$ treatment at 70 °C for 30 min and sintered at 500 °C for 30 min. A TiO_2 (15–25 nm) main layer was applied using 3 M double-tape and heated at 130 °C for 15 min. An overlayer of scattering layer paste (G2, 500 nm) was applied with a single tape (3 M). Finally, the samples were sintered at 500 °C for 30 min to remove the binders and formation of connections in the TiO_2 layer. The sintered TiO_2 films were again subjected to $TiCl_4$ treatment, same as blocking layer treatment. The photoanodes were immersed in a 0.5 mM N719 dye solution for 24 h. The dye-adsorbed photoanodes were coupled with the counter electrode using a spacer and separator, as reported by others [24].

The liquid electrolyte was filled between the electrodes, which served as an intermediate shuttle to complete the electrochemical cycle. The electrolyte solution was composed of 0.6 M 1-butyl-3-methyl-imidazolium-iodide and 50 mM iodine, 0.5 M 4-*tert*-butyl pyridine, and 0.1 mM lithium-iodide in acetonitrile solvent.

2.5. Assembled NGQDs for counter electrode

To ensure proper orientation of NGQDs, fast drying of the solvents is crucial; therefore, the NGQDs coatings were dried in a vacuum oven at 90 °C. Initially, we compared the orientation behavior of different sizes of NGQDs by adding the antisolvent dimethylacetamide, as shown in Fig. 1. NGQDs with the strongest orientation ability (smallest nano-assemblies by phase separation) were added to the hGO solution to investigate the orientation of hGO via phase separation of NGQDs. The ratio of hGO to NGQDs was maintained at 4:1 (as optimized by others [17]) in a solvent mixture of water (95%) and DMA (5%). The maximum porosity and conductivity of the composite structure can be achieved by using 25% inclusion of NGQDs [17]. The solution formed by the uniform dispersion of all components was drop-casted on the FTO glass to fabricate the counter electrode for DSSCs. The composite structure of NGQDs (without size separation) and hGO was labeled as NGQDs@hGO. The composite structures of separated NGQDs (GD-1/10/50) were labeled according to the sizes of NGQDs; for example, the GD-1 and hGO composite is labeled GD-1@hGO. Before employing the electrode in DSSCs, all electrodes were reduced by thermal annealing at 300 °C under a nitrogen environment. Thermal reduction restores the conductivity in the porous carbon network, enabling it for electrocatalytic applications.

To fabricate the conventionally used Pt electrode, we drop-casted 5 mM chloroplatinic acid solution on the FTO glass. After drying, the samples were sintered at 400 °C for 30 min. Pt samples were coupled with a photoanode to achieve reference DSSC.

2.6. Characterizations

The shape and size of the synthesized NGQDs were analyzed using a transmission electron microscope (TEM JEOL JEM-2100 F). Wide-angle X-ray diffraction (WAXD) analysis was performed to examine the crystal structure of the NGQDs in the 2θ range of 10°–80°. The X-ray source of Cu Kα (Rigaku D/MAX-2500) manufactured by Rigaku Denki was used at an acceleration voltage of 40 kV. Graphitic arrangements and defects were surveyed using a Raman spectrometer (JASCO, Japan) equipped with a

monochromatic green laser for excitation. A Fourier transform infrared (FTIR) spectrophotometer (Thermo Fisher Scientific Inc.) was used to evaluate the variation in functional groups. Atomic composition and bonding were further probed using an X-ray photoelectron spectroscopy (XPS) (Multilab ESCA lab-system VG, Thermo-Scientific, USA). The absorbance spectrum of the NGQDs was studied using a UV–visible absorbance spectrometer (Shimadzu, Japan). The fluorescence spectrum was analyzed using a fluorescence spectrophotometer (SCINCO, Korea).

The surface morphology of the assembled GQDs was analyzed using a field emission electron microscope (FE-SEM; JEOL JSM 670F) with an acceleration voltage of 15 kV. To enhance the imaging quality, the samples were subjected to Pt sputtering for 1 min before performing the SEM test. The electrochemical response of the electrodes was studied using a three-electrode system on a biological workstation. A scan rate of 10 mV/s was used to test the electrocatalytic activity of the carbon electrodes in the potential range of 1.0 to (−0.2) V. The performance of the solar cell was measured under a simulated light source (1 sun), calibrated with a standard (K101-Lab 20) measuring unit (Mac Science, Korea). The surface area of the electrodes was approximated using the Brunauer–Emmett–Teller (BET) analysis of nitrogen adsorption and desorption (Quantachrome Autosorb-6 systems). Variations in surface roughness attributable to the assembly of NGQDs were measured using tapping mode atomic force microscopy (AFM), XE-70-(Park-systems).

3. Results and discussion

The catalytic activity of carbon materials strongly depends on the surface area and porosity of the film [25]. This effect is critical in the case of 2D carbon (rGO) films, owing to the unwanted stacking of rGO sheets in the film form. In the stacked structure, the electrocatalytic activity is limited by the diffusion and transport of electrolyte ions, as depicted schematically in Fig. S1. Although rGO is enriched with abundant active sites; however, electrolyte transport limits the overall electrocatalytic activity of the coating. To solve this problem, we propose a highly porous orientation of hGO nanosheets using the phase separation of NGQDs, as shown schematically in Fig. 1. Different sizes of NGQDs were separated using different sizes of dialysis membranes and their aggregation kinetics were studied (Stage 1 in Fig. 1). The porous self-assembly of NGQDs by phase separation was optimized for the different sizes of NGQDs, which can potentially serve as a soft template for the orientation of hGO sheets (Stage 2 in Fig. 1). The orientation strength of different NGQDs was determined using the smallest size of nanostructures formed; the smaller dimension of nano-assemblies is related to stronger orientation ability or phase separation. The antisolvent for the phase separation was optimized and NGQDs with the strongest orientation were incorporated into hGO sheets to orient the hGO sheets in a highly porous 3D network (Stage 3 in Fig. 1). The porous orientation of hGO improves the electrocatalytic performance, which was confirmed by the superior performance of the DSSC fabricated by the associated counter electrode (Stage 4 in Fig. 1).

NGQD-assisted orientation of hGO is a facile method for the orientation of hGO and is scalable for uniform coating over a large area. In addition to orientation, NGQDs reinforce the electrocatalytic activity of hGO by improving the conductivity and increasing the content of active sites for the electrochemical reaction [17–19,26]. In comparison, other solid templates, such as Ni foam, nanoparticles, and polymer substrates, require harsh chemical etching and thermal annealing for their removal after the porous orientation of rGO sheets [9]. Here, for the first time, we identified a suitable size and solvent for the strong orientation of NGQDs, which can also be used for the porous orientation of other nanomaterials.

The size distribution of NGQDs was confirmed using TEM, for instance, by using 1 kDa membrane, GD-1 was separated, which had the smallest size of ~3.5 nm (Fig. 2(a)). Similarly, by using dialysis membranes of 10 kDa and 50 kDa, slightly larger sizes of NGQDs were separated, as clearly observed from the TEM analysis of GD-10 and GD 50 in Fig. 2(b and c), respectively. The average size distribution of GD-1 (~3.5 nm), GD-10 (5–6 nm), and GD-50 (10–12 nm) are shown in Figs. S2(a,b,c). The crystalline core and amorphous edges of the NGQD structure can be observed when analyzed under high resolution (Fig. S3). This difference can be attributed to the higher functionality of edges as compared to the core/basal plans [27,28]. Mutual repulsion between the highly functional groups attached to the edges causes a slight expansion in the basal planes, which causes a shift of the XRD peak of NGQDs to lower angles relative to hGO or GO nanosheets (Fig. 2(d)) [29]. Both hGO and NGQDs showed characteristic XRD peaks at angles (2θ) of ~25° and 44°, which correspond to the (002) and (100) diffraction planes, respectively [29]. Compared to hGO, the XRD peaks of NGQDs are of low intensity and broad, which can be attributed to their small size and broad size distribution.

The structure of NGQDs was further probed using Raman analysis, which exhibited the D-band and G-band associated with graphitic/crystalline regions and surface defects. Interestingly, the $I_{D/G}$ value of NGQDs was 1.10 (Fig. 2(e)), which indicates that NGQDs possess a significant amount of surface defects [30]. Surface defects originate from the higher surface oxidation or surface functional groups, as confirmed by FTIR analysis (Fig. 2(f)). Higher content of OH/NH and C–N bonds was observed for NGQDs compared to that of hGO, as highlighted in Fig. 2(f). Defect-rich and highly functional surfaces of carbon materials are attractive for superior electrocatalytic activity [31].

The atomic compositions of both NGQDs and hGO were studied using XPS, as shown in Fig. 2(g). Three main peaks for C1s, N1s, and O1s can be observed at binding energies of 285 eV, 400 eV, and 533 eV, respectively. Typically, both hGO and NGQDs had the same building blocks; however, NGQDs with a smaller size can accommodate a higher content of oxygenated and nitrogenated functional groups. Therefore, the concentration of N1s and O1s is higher for NGQDs compared to that for hGO. The above characterizations prove that NGQDs were successfully synthesized and possess a highly functional surface compared to hGO or GO.

The difference in size imparts a variation in the optical properties of NGQDs by varying the quantum confinement effect and surface states of the NGQDs. To confirm this, we analyzed UV–visible absorbance for different-sized NGQDs, as shown in Fig. 2(h). The UV–visible spectroscopy showed an absorbance peak around 330 nm, which arises from n-π* excitations in the UV spectrum [32]. In addition, the n-π* transitions have a shoulder peak extending in the visible spectrum, which is due to surface functional groups attached on the surface [32]. The surface functional groups generate intermediate energy levels (surface states) between the highest occupied molecular orbital (HOMO) and lowest unoccupied molecular orbital (LUMO) energy level. Excessive surface states increase the probability of electron transitions at lower energies. Amongst different sized NGQDs, GD-1 exhibited higher absorbance in the lower energy spectrum, which is associated with their higher surface functionality [16,27]. The smaller size of GD-1 provides a higher surface area for accommodating the higher content of surface functional groups [33,34].

The fluorescent emission of NGQDs was examined to gain insight into differences in the electronic structure according to size. The emission of GD-1, GD-10, and GD-50 was centered at 499 nm, 485 nm, 519 nm, under the excitation wavelength of 365 nm (Fig. 2(i)), respectively. Green color emission for NGQDs could be observed under a 365 nm UV lamp, as shown in the inset of Fig. 2(i). The Stokes

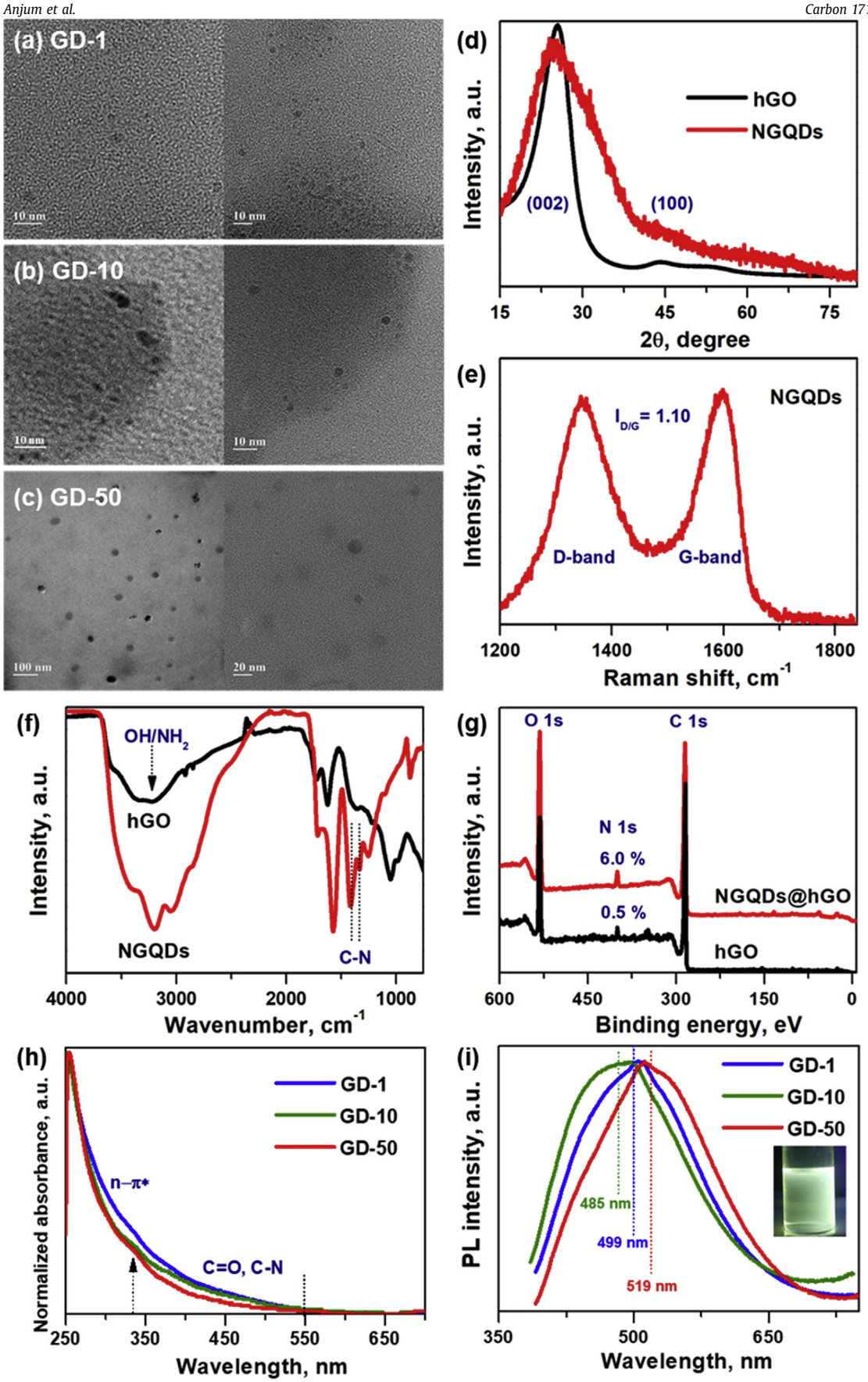

Fig. 2. TEM micrographs of (a) GD-1, (b) GD-10, and (c) GD-50, showing the difference in the size of NGQDs. Characterizations to confirm the synthesis of NGQDs and hGO using (d) XRD, (e) Raman analysis, (f) FTIR, and (g) XPS survey. Evaluation of optical properties using (h) UV–visible absorbance and (i) fluorescence spectrophotometry. (A colour version of this figure can be viewed online.)

shift of NGQDs was observed to be size-independent, which is a common feature when fluorescence is strongly affected by the surface states [35]. For instance, the highest Stokes shift of GD-50 is due to its longer conjugation length and associated lower bandgap. In contrast, GD-1 shows the second-highest Stokes shift due to its superb surface functionality [36]. The functional group-rich surface of GD-1 generates additional surface states, which reduce the HOMO-LUMO gap. Lowering of the bandgap is responsible for higher Stokes shift in GD-1, as compared to GD-10 [36].

The self-assembly behavior of NGQDs was strongly dependent on the size of NGQDs as different shapes of assemblies can be observed for GD-1/10/50. The film formed by NGQDs at room temperature was uniform (Fig. S4); however, rapid evaporation induced well-defined nano-architectures in the NGQD films, as shown in Fig. S5. The GD-1 film showed a nanowall shape, with an occasional vertical alignment of rod-like structures (Fig. S5(a)). The high-resolution images show a highly crumpled and slightly vertically aligned structure. The height of an individual wall was approximately 10 μm, as observed from the cross-sectional view of the GD-1 film. In contrast, GD-10 showed a highly dense and porous shape resembling a sea sponge, as shown in Fig. S5(b). The nano-sponge formed a hyperbranched fractal porous network on the substrate. The length of each sponge rod was approximately 250 nm and the width varied between 30 and 50 nm, as highlighted in Fig. S5(a). Unlike the highly intricated shapes formed by GD-1 and GD-10, the film formed by GD-50 was uniform, as shown in Fig. S5(c). As GD-50 contained a significant proportion of larger-sized (>12 nm) GO sheets, its orientation could not be observed solely by fast drying. Nevertheless, hierarchically porous nanowalls and sponge-like structures could be observed using the NGQD mixtures. It is interesting to note that the presence of GD-50 causes the formation of thicker structures compared to separated GD-1/10. The differences in the sizes of the nano-shapes formed is the evidence of the significant effect of NGQDs' size on aggregation kinetics.

The strength of NGQD assembly by fast drying is sufficient for their self-orientation; however, not strong enough to orient the GO/hGO nano-sheets. For instance, GD-10 exhibited the smallest dimensions of the nano-sponge shape; however, in the presence of hGO nano-sheets, a smooth film with slight cracks appeared, as shown in Fig. S6. Pure NGQDs-based films show a high charge transfer resistance; therefore, incorporation of nano-sheets is crucial to achieving the required charge conductivity. For this purpose, we strengthened the orientation ability of NGQDs using antisolvent, to ensure the orientation of the hGO nano-sheets. To achieve a strong phase-separation, we selected DMA as an antisolvent. Propanol was previously optimized as an antisolvent, where butanol caused the formation of thicker nanostructures [6]. However, the immiscibility of butanol limits its use as an antisolvent [6]. The boiling point of propanol (antisolvent) is lower than that of water (solvent); therefore, the minimum dimensions of the nano-assembly were 2–5 μm. Using DMA as an antisolvent, stronger phase separation can be achieved because the boiling point of DMA is much higher than that of water. Additionally, unlike butanol, DMA has better miscibility in water; hence, a stronger antisolvent effect can be achieved.

The antisolvent-assisted nanoarchitecture varies significantly for different sizes of NGQDs, as shown in Fig. 3. GD1 exhibited a highly porous interconnected network of fractal nanorods, as shown in Fig. 3(a). The densely packed nano-whiskers are assembled in a nanoflower pattern, as labeled in the high-resolution image of GD-1 assembly. The length and width of individual nano-rod were approximately 1 μm and 3 μm, respectively. The strong anti-solvent effect led to the formation of a nanofoam-like structure throughout the film formed by GD-1. Under the same conditions for GD-10, a nanowall-like structure was formed, as shown in Fig. 3(b). The thickness of the individual wall was approximately 1.5 μm, as shown in Fig. 3(b). In contrast to GD-1, the nanowall formation in GD-10 was less uniform as no orientation was observed in some portions. Similarly, no orientation was observed in GD-50 even with the addition of antisolvent, as shown in Fig. 3(c). Analyzing the GD-50 film at high resolution, a nanoporous membrane-like structure was observed. The NGQD mixture formed a sea urchin-like structure in the presence of an antisolvent, as shown in Fig. 3(d). Such orientation probably originated from the compact ball formation by GD-50; however, GD-10 and GD-1 produced nanorods on the surface. It is important to note that the assemblies formed by the NGQD mixture are not uniform throughout the whole surface (unlike GD-1), as observed in the low-resolution images in Fig. 3(d). In addition, the nano-whiskers formed by NGQDs mixtures have thicker dimensions, which can be attributed to the weaker antisolvent effect in the mixture form. By comparing the antisolvent-assisted assemblies of different sizes, the phase separation of GD-1 can be considered optimum, as it shows smallest dimensions. Therefore, GD-1 was selected for the orientation of the hGO sheets.

Fig. 4 shows the porous network formed by the GD-1 and hGO composite (GD-1@hGO) structure. The structure exhibited high porosity at low resolution, as shown in Fig. 4(a). The porous framework showed a slight overlap of GD-1 rods and hGO nanosheets, as highlighted in Fig. 4(b). The rods formed by the phase separation of GD-1 provide support for the 3D orientation of the hGO sheets. The porous network formed by the phase separation of GD-1 slightly varied in the presence of hGO sheets. Mutual hydrophilic interactions between GD-1 and hGO reduced the antisolvent effect relative to the pure GD-1 film. However, by optimizing the concentration and size of NGQDs, a hierarchically porous structure could be achieved. It is interesting to note that although hGO sheets coalesce with GD-1, the porosity is retained because of the holes formed in hGO. For instance, Fig. 4(c) highlights the porous nature of hGO sheets, which provides additional channels for electrolyte transport. In contrast, the use of rGO (without holes) could block the pores of the network. The limited porosity of rGO hampers its electrocatalytic performance as the exposed area of rGO sheets on the top surface can only participate in the electrochemical reaction (Figs. S7(a–c)). The electrolyte can only diffuse in the film through the edges of the rGO sheets; hence, the overall reaction is diffusion limited. The long diffusion paths of the rGO film are depicted in Fig. S7(d). In contrast, the hGO provides a larger number of active edge sites for the electrochemical reaction, as highlighted in Fig. S8(a). Furthermore, the hGO sheets possess micro and macro holes (Figs. S8(b–d)), which can effectively reduce the diffusion length. In addition to holes in the hGO sheets, the film formed by hGO sheets has excessive cracks, which further assists in electrolyte transport. Compared to rGO, hGO facilitates faster electrolyte transport, as schematically shown in Fig. S8(e). Although the electrolyte flow is improved in the hGO nanosheets, there is still room for further improvements by its 3D porous orientation. The porous orientation of hGO sheets provide superior exposed surface area with a high-speed flow of electrolyte (Fig. 4(d)).

The enhanced electrocatalytic activity attributable to the orientation of hGO was confirmed through cyclic voltammetry using a three-electrode system. In brief, two oxidation peaks and two reduction peaks were observed at positive and negative potentials (Fig. 5), respectively. The first-oxidation peak and second-reduction peak mimic the oxidation-reduction dynamics of DSSCs; therefore, the electrocatalytic activity parameters were considered according to the respective peaks. The oxidation and reduction reaction of the iodide electrolyte are presented in the insets of Fig. 5(a). Important parameters for calibrating the electrocatalytic activity are as follows: (1) current density of the second reduction peak (I_{red}) and (2) the potential difference between the

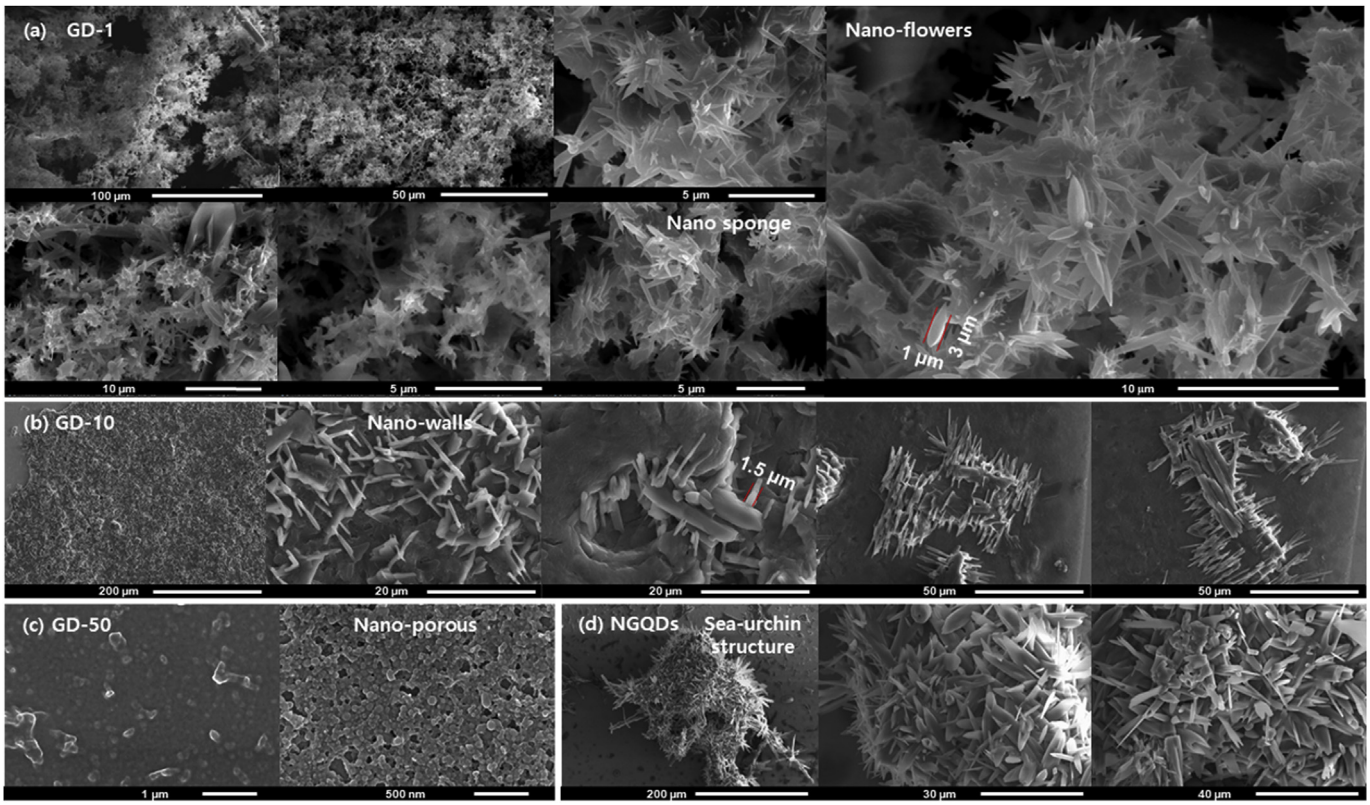

Fig. 3. SEM micrographs of antisolvent assisted assemblies formed by (a) GD-1, (b) GD-10, (c) GD-50, and (d) NGQDs (mixture).

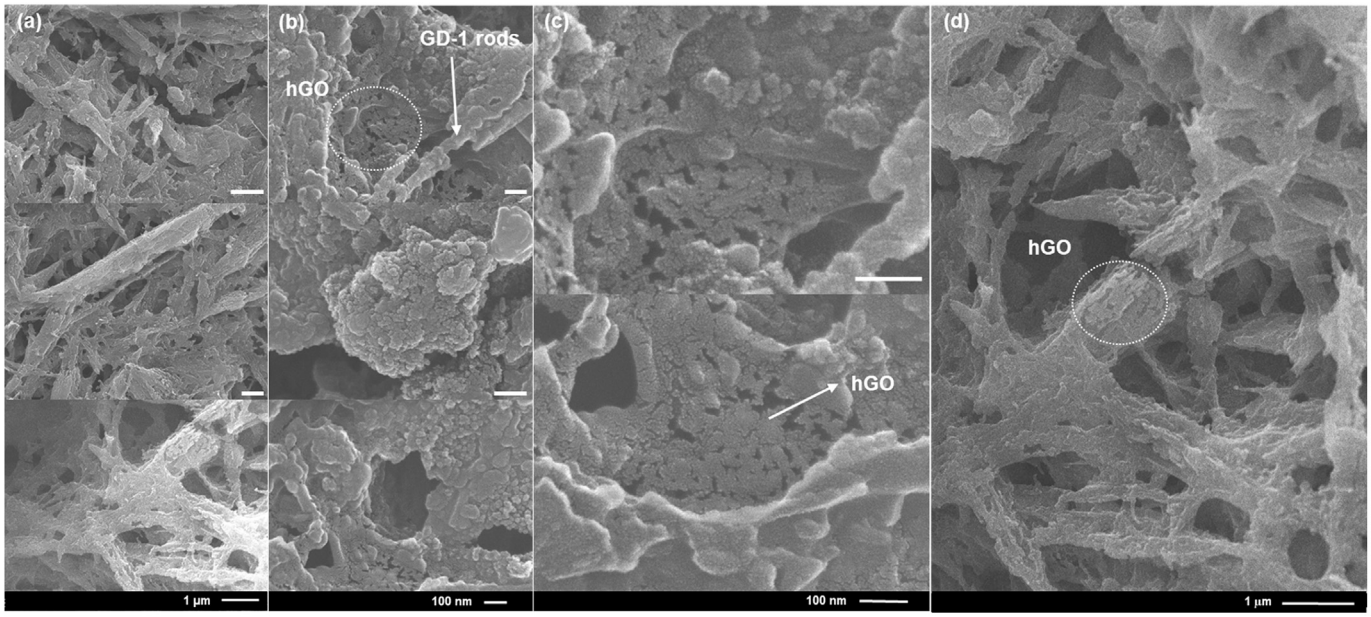

Fig. 4. Highly porous assembly of hGO formed by the phase separation of GD-1: (a) low-resolution image showing micro-porous network (inset scale bar 1 μm) and (b, c) high-resolution morphology of GD-1 and hGO (inset scale bar 100 nm). (d) Hierarchically porous assembly of composite showing micro and mesoporous structure.

first oxidation and second reduction peaks (E_{PP}) [37]. A higher intensity of I_{red} with a lower E_{PP} value corresponds to the superior electrocatalytic activity of the electrode.

In order to test the effectiveness of the hGO and NGQDs composite, we compared its electrocatalytic activity with other intermediate stages of composite synthesis (Fig. 5(a)). Pure rGO sheets showed a limited I_{red} due to the limited exposed surface area available for direct electrochemical reaction. Compared to the sluggish kinetics of stacked rGO sheets, the electrocatalytic activity of the hGO electrode was significantly improved. The formation of holes and cracks

enabled higher electrolyte flow, providing higher current densities [38]. It is important to note that although the hGO electrode showed improved current density, the variation in E_{PP} was negligible. On the other hand, the incorporation of NGQDs improved both I_{red} and E_{PP} simultaneously, as tabulated in the inset of Fig. 5(a). The incorporation of conductive hGO nano-sheets is critical for imparting superior electrocatalytic activity, as the pure NGQDs film exhibited almost negligible electrocatalytic activity similar to FTO glass (Fig. S9). Although NGQDs have a highly active surface, pure NGQDs film has poor conductivity; hence, charge transport is the rate-limiting step. We studied the size-dependent electrocatalytic activity of the hGO and GD-1/10/50 composite structure in comparison with the mixture of NGQDs (Fig. 5(b)). As the orientation of hGO sheets is negligible when using GD-10/50, we compared the uniform coating of all NGQDs sizes (without adding antisolvent). The current density of NGQDs was inversely related to the size of NGQDs; for instance, the highest I_{red} was recorded for the smallest sized NGQDs (GD-1). In contrast, E_{PP} exhibited a similar trend to the Stokes shift, GD-10 showed a higher E_{PP}, which is associated with their high bandgap [39]. GD-1 outperformed NGQDs of other sizes due to its excessive surface functionality, higher surface area, and comparatively lower bandgap [40]. The parameters determining the electrocatalytic activity of the GD-1/10/50 composites are tabulated in Fig. 5(b).

The incorporation of GD-1 improved the performance of hGO;

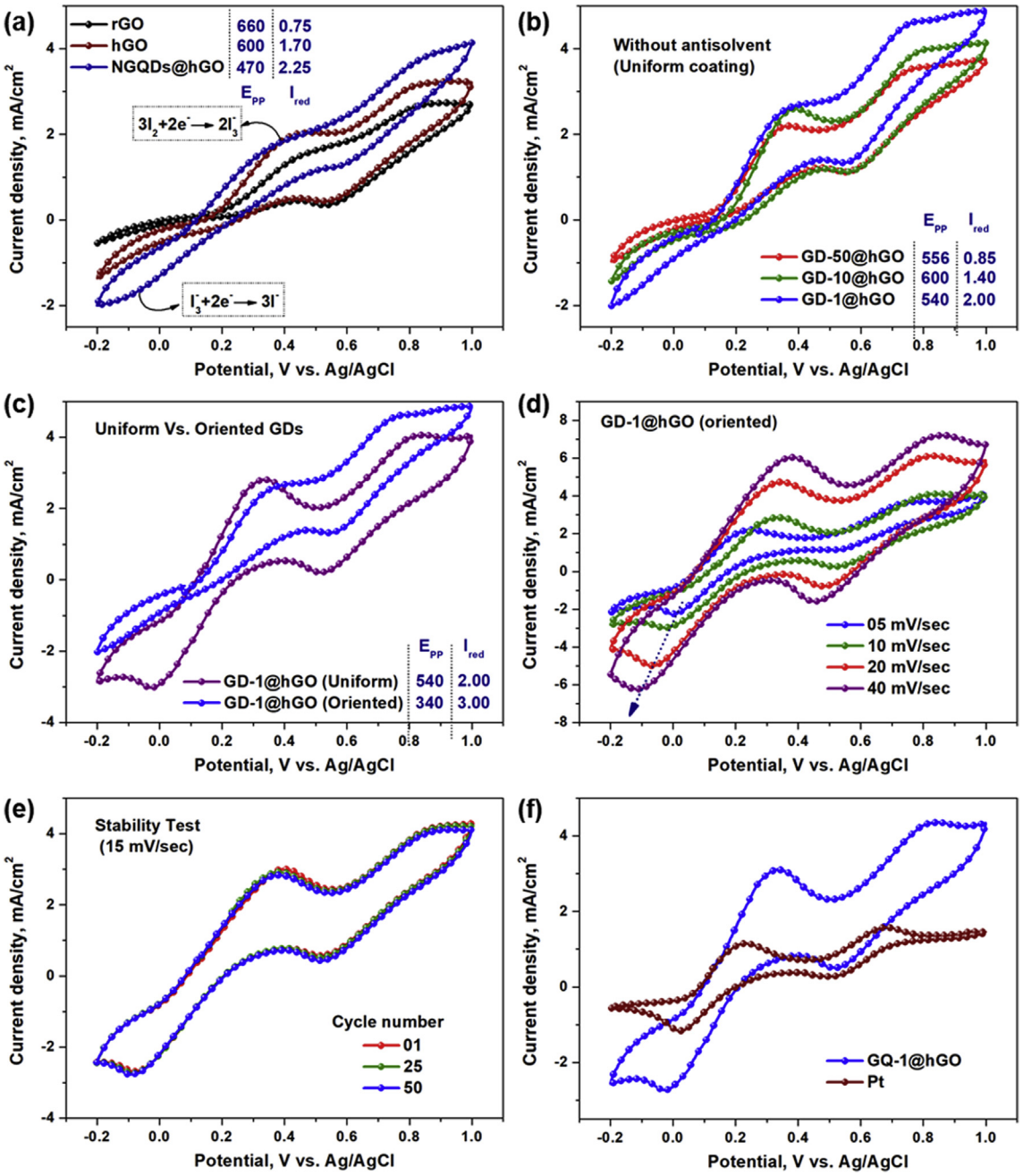

Fig. 5. Evaluation of electrocatalytic activity using cyclic voltammogram: (a) comparison of rGO, hGO, and NGQDs@hGO, (b) comparison of different sizes of NGQDs, and (c) effect of orientation. Cyclic voltammogram of oriented GD-1@hGO (d) at different scan rates, and (e) for 50 cycles. (f) Comparison of electrocatalytic activity of GD-1@hGO with Pt coated FTO glass electrode. (A colour version of this figure can be viewed online.)

however, GD-1 was not completely exposed to the redox reaction in the uniform film. For this purpose, the antisolvent-assisted 3D porous assembly of the GD-1 composite (oriented) was compared with the uniformly coated (without antisolvent) GD-1 composite, as shown in Fig. 5(c). The porous network formed by the antisolvent provides the maximum exposed surface area of GD-1 to participate in the redox reaction. Therefore, the electrocatalytic activity of the oriented composite structure was two times higher than that of the uniform coating. Categorically increased I_{red} and E_{PP} were observed in the 3D orientated composite of the hGO sheets, as tabulated in Fig. 5(c). Moreover, the oriented composite structure retained the electrocatalytic performance even at high scan speeds, as shown in Fig. 5(d). Proportionate increase in E_{PP} and I_{red} was observed with increasing scan rate, as commonly observed in porous carbon materials [25,41]. The retention of electrocatalytic activity at high scan speeds implies that the high porosity of the composite enables the high-speed flow of electrolytes throughout the composite structure [37]. Furthermore, we tested the electrocatalytic activity for 50 continuous cycles at 15 mV/s, as shown in Fig. 5(e). The decrease in electrocatalytic performance was negligible, thereby verifying the stability of the oriented hGO sheets. Unlike metallic catalysts, the long-term stability of carbon materials is a known characteristic attributable to their high corrosion resistance against harsh electrolyte environments. The long-term stability of the electrocatalyst is linked to the long-term performance of the DSSC. The stability of the composite structure provides a competing edge over the conventionally used Pt electrode. Besides, the electrocatalytic performance of the GD-1@hGO composite structure is comparable to that of the Pt electrode, as shown in Fig. 5(f). In conclusion, our proposed oriented composite structure integrates suitable porosity, stability, and catalytic activity in a single structure.

The enhancement of electrocatalytic activity of oriented composite structure is attributed to the increase in the exposed surface area. Moreover, the new surfaces provided by hGO and NGQDs are more functional and defect-rich compared to that of pure rGO, which promotes electrocatalytic activity [4]. Specifically, the doped nitrogen plays a key role in strengthening the electrolyte and carbon composite interface. The slightly higher electronegativity of surface nitrogen creates a partially negatively charged zone [42]. This in turn induces a positive charge on the neighboring carbon atoms. The charge redistribution effect generates additional electrostatic interactions with pseudo-charged electrolyte ions, accelerating the redox cycle [42]. In addition to tuning the surface reactivity, the conjugated (pyridinic) nitrogen in the core of NGQDs adds extra electrons to the p-π conjugating electron cloud of the composite structure. A higher density of electrons near the Fermi level facilitates electron transitions at a lower potential, decreasing E_{PP} [43]. Overall, the enhancement of electrocatalytic activity by NGQDs is attributable to the increased surface area (by orientation) and surface reactivity or modulation of the electronic structure (by nitrogen doping). The results of electrocatalytic activity suggest that oriented GD-1@hGO outperforms all the other composite structures. Considering GD-1@hGO as an optimized composite sample, we compare its performance with the controlled rGO and hGO samples in the next section.

From the porous, interconnected network observed in the SEM analysis, the composite structure can be expected to provide lower diffusion paths and associated lower charge transfer resistance. The porous structure can reduce the electron flow and electrolyte diffusion paths in the radial symmetry of the electrode, thereby suppressing the diffusion dependent internal resistance. To confirm

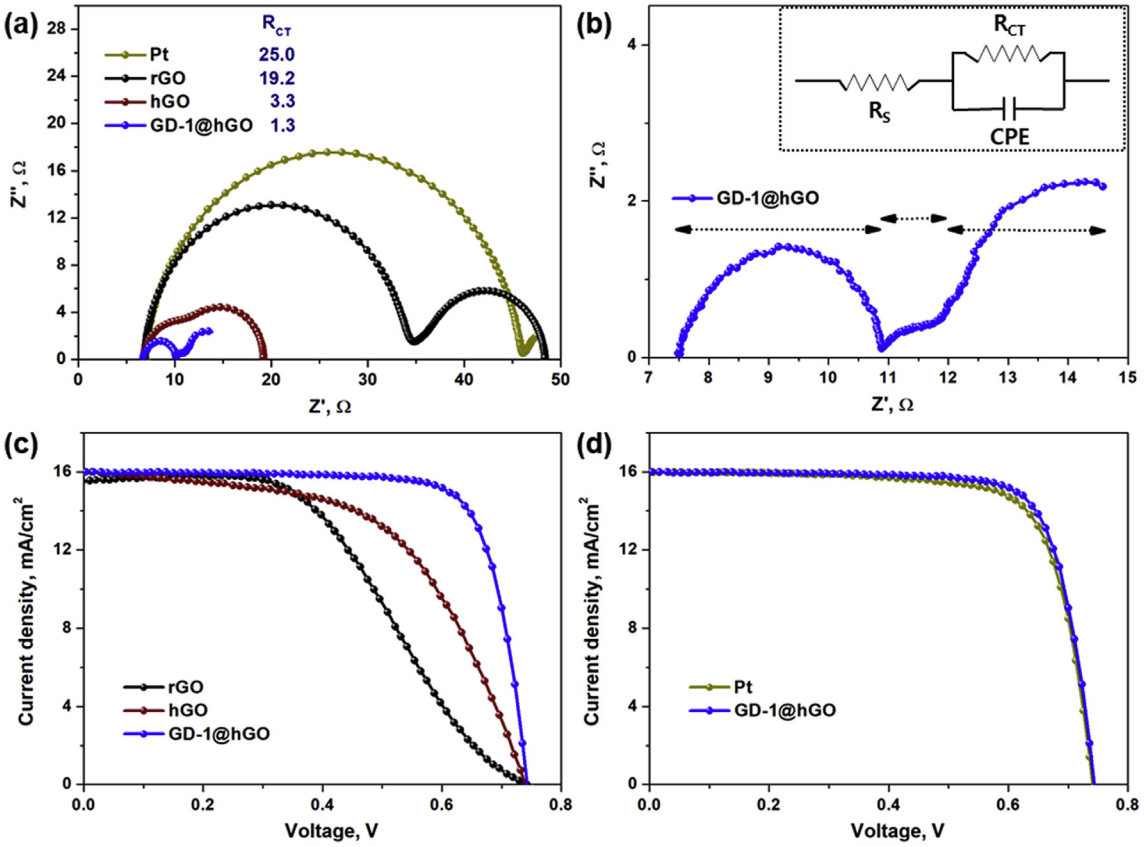

Fig. 6. (a) Nyquist plot of rGO, hGO, NGQDs@hGO, and Pt electrode (inset table shows variations in R_{CT}). (b) Nyquist plot of NGQDs@hGO, highlighting different sections. J-V curves for (c) carbon electrodes, and (d) comparison of optimized sample with Pt electrode. (A colour version of this figure can be viewed online.)

this effect, the charge flow dynamics of the composite structure were studied through electrochemical impedance spectroscopy, which was performed with a symmetrical cell configuration to avoid impedance contributed by the photoanodes (Fig. 6(a and b)). The x-intercept of the Nyquist plot accounts for the series resistance R_S, whereas the height along the y-axis is related to the charge transfer resistance (R_{CT}) [44]. The lower values of both R_S and R_{CT} are responsible for the lower internal resistance of DSSC [44]. Fig. 6(a) shows that the difference in R_S was almost negligible in all samples because the conductivity of the substrate used was similar. In contrast, the introduction of porosity in the structure led to a notable difference observed in R_{CT}. For example, the R_{CT} of oriented GD-1@hGO was fifteen and three times lower than that of conventional rGO and hGO structures, respectively. Similarly, the R_{CT} of the composite structure was dramatically (~twenty-five times) lower than that of the Pt electrode. The Nyquist plot of the oriented GD-1@hGO in Fig. 6(b) shows three main sections. The height of the first semicircle is attributable to the initial charge transfer barrier at the electrode and electrolyte interface. The second semi-circle is associated with electrolyte diffusion throughout the porous network formed by the active materials [45]. The third semi-circle is related to the internal impedance of the electrolyte itself [45]. Specifically, the suppressed second semicircle is evidence of porosity introduced in the hGO network by the incorporation of GD-1. In contrast, in pure rGO and hGO films, the diffusion-controlled impedance and initial transfer barrier are the rate-limiting steps.

The reason for the dramatic decrease in the R_{CT} can be attributed to the porosity introduced by the inclusion of GD-1. The stacking of hGO sheets was radically avoided by their 3D orientation, which provided unobstructed channels for the diffusion of electrolyte ions. Rapid infiltration of the electrolyte in the porous network formed by GD-1@hGO enables high-speed diffusion of the electrolyte [46]. Moreover, the diffusion distance of the electrolyte is drastically reduced in the porous network, which in turn reduces the diffusion impedance in the radial symmetry of the electrode [46]. The highly functional edges of hGO and GD-1 are directly exposed in the porous network, which provides strong capillary action for electrolyte transport throughout the structure. In addition, the dramatically lower height of first semicircle of the composite structure indicates the extremely low initial charge transfer barrier required to initiate the redox reaction on the interface [47]. The low initial charge transfer barrier is due to the high surface reactivity of the electrode caused by surface charge redistribution, as explained in the above section.

Higher electrocatalytic activity combined with low charge transfer resistance makes the designed composite structure suitable for counter electrode applications. To evaluate the efficacy of the composite structure as a counter electrode, we coupled the photoanode with the carbon electrodes and analyzed their photovoltaic performance. The performance of the solar cells fabricated with the carbon electrodes is given in Fig. 6(c) and Table 1. The performance of the DSSC widely varied with increasing porosity of the counter electrode materials. In general, the fill factor (FF) was responsible for the variation in the efficiency of the solar cell; other parameters showed almost negligible variation. The enhanced FF can be attributed to the dramatic decrease in the internal resistance of the solar cells caused by the 3D orientation of the structure (as clearly indicated by the R_{CT} value in Table 1). The lower internal impedance of the solar cell is responsible for the improvement of FF and overall photovoltaic performance. Furthermore, the high mobility of electrolyte ions and their rapid reduction by the designed electrocatalyst ensured abundant reduced electrolyte ions near the dye molecules. Hence, the completion of the electrochemical cycle in the DSSC can be attributed to the efficient reduction by the proposed electrode. In contrast, the complex electrolyte flow and high charge transfer resistance of the rGO electrode affect the FF and performance of the DSSC. The enhancement of the photovoltaic performance and increase in the BET surface area had a direct correlation, as shown in Table 1. This indicates that the enhanced surface area and associated electrolyte dynamics are critical determinants of the enhanced performance of our proposed system. The performance of the DSSC was comparable to that of the Pt counter electrode, as shown in Fig. 6(d) and Table 1.

3.1. Mechanism of size-dependent assembly and catalytic activity

The mechanism of 3D assembly and associated enhanced electrocatalytic activity was investigated to determine the reason for the size-dependent response in NGQDs. Fig. 7(a) explains the phase separation mechanism of NGQDs, where DMA serves as an antisolvent, thus forming the NGQD-poor phase (yellow color); in contrast, the NGQD-rich phase (blue color) formed in water because water is a good solvent for NGQDs. The poor phase formed random pores in the structure upon drying as the concentration of NGQDs was almost negligible in this phase. In contrast, the NGQD-rich phase formed an interconnected network owing to the high concentration of NGQDs. In conclusion, the difference in the solubility of NGQDs in the solvent mixture is primarily responsible for the porous orientation of NGQDs [48].

The phase separation mechanism was different for different sizes of NGQDs as observed in the phase-separated assembly of DMA and water mixture via TEM. The TEM analysis revealed a clear difference in the assemblies of GD-1, GD-10, and GD-50, as shown in Fig. 7(b–d), respectively. The size of the phase-separated assemblies increased linearly with increasing NGQD size. For instance, the dimensions of the smallest units of GD-1, GD-10, and GD-50 were approximately 25 nm, 150 nm, and 700 nm, respectively. The difference in the aggregate size of each NGQD can be attributed to the variation in the antisolvent effect with NGQD size. In addition, the orientation shape also significantly varied with NGQD size; for example, GD-1 showed a thin porous film-like structure, whereas GD-10 and GD-50 exhibited a stacked form of hollow and solid structure, as depicted schematically in the inset of Fig. 7(b–d).

The formation of such shapes can be interpreted on the basis of J-type, JH-type, and H-type aggregation of GD-1, GD-10, and GD-50, respectively. The aggregation of NGQDs is mainly driven by dipole-dipole interactions, hydrogen bonding, solvent interactions, and solubility difference of antisolvents [49]. Specifically, size differences lead to significant differences in interactions between NGQDs

Table 1
Summary of the photovoltaic performance parameters for different electrodes.

	BET Area (m^2/g)	R_S (Ω)	R_{CT} (Ω)	V_{OC} (V)	J_{SC} (mA/cm^2)	F.F (%)	η (%)
rGO	60	7.5	19.0	0.74	15.8	44.5	5.1
hGO	135	7.5	3.3	0.74	16.0	57.0	6.7
GD-1@hGO	353	7.5	1.3	0.74	16.0	77.5	9.1
Pt	N/A	7.5	25.0	0.74	16.0	75.0	8.8

*The values of R_S and R_{CT} are summarized from electrochemical impedance spectroscopy.

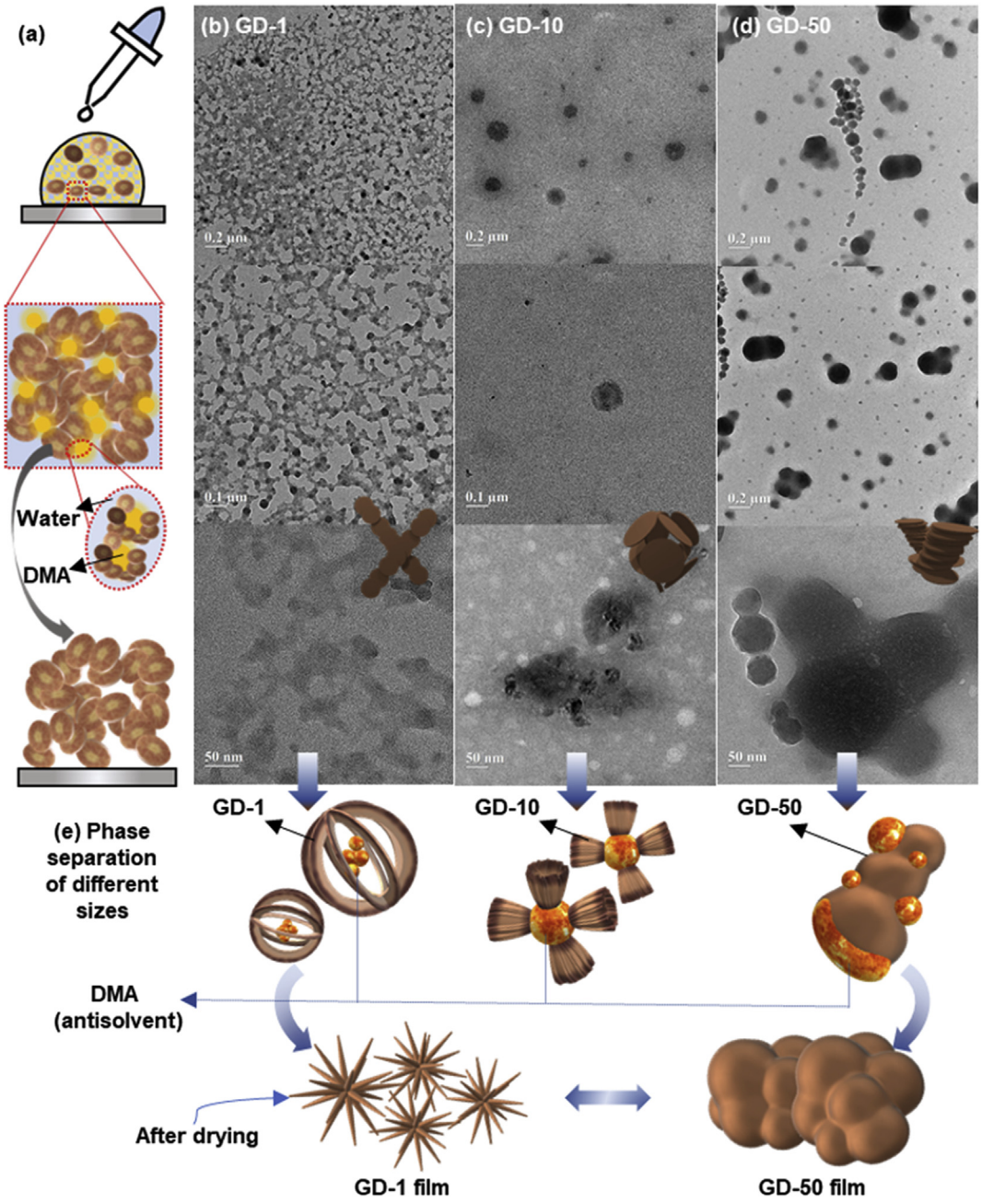

Fig. 7. (a) Schematic illustration of the phase separation mechanism in NGQDs and associated porous orientation. (b,c,d) TEM analysis of aggregates formed in GD-1, GD10, and GD-50; inset shows a schematic representation of NGQD assembly mechanism. (e) Approximation of aggregation kinetics in different sized NGQDs, and the difference in their assemblies after drying. (A colour version of this figure can be viewed online.)

and the antisolvent, as depicted schematically in Fig. 7(e) (yellow color for antisolvent). Larger-sized NGQDs (GD-50) have a higher proportion of graphitic core (non-polar nature), whereas GD-1 has a higher edge ratio (polar nature) [3]. The difference in the polarity of the graphitic plan and edge imparts a surfactant/amphiphilic nature to NGQDs similar to GO nanosheets. By increasing the graphitic planes content or non-polar nature, the mutual compatibility between NGQDs and antisolvent is increased, and vice versa. As shown in Fig. 7(e), GD-1 exhibits the least interaction with the antisolvent, and its phase separation is strong, which can be attributed to the highest content of functional edges. In the case of GD-10, although the graphitic planes tend to dissolve in the antisolvent, the edges are retained in the water. Compared to GD-1, the solvent interactions are slightly improved in GD-10 owing to a slightly higher proportion of graphitic planes. With the lowest content of functional edges, the antisolvent effect is negligible in GD-50, and consequently, the overlap of DMA is the highest (as depicted schematically in Fig. 7(e)). Considering the amphiphilic nature of NGQDs, the finer and thicker assemblies in the GD-1 and GD-50 solid films are depicted in Fig. 7(e).

The slightly polar graphitic plane and highly functional edges of graphene oxide have also been utilized previously to prepare porous Pickering emulsions and breath free assemblies using organic antisolvents, such as toluene [50,51]. However, such methods require complex processing for the complete orientation of GO nanosheets; for example, the continuous flow of high humidity and grafting of

polymers onto GO [50,51]. The size of the GO nanosheets is also an important parameter for the formation of Pickering emulsions; as larger GO sheets have a higher graphitic portion, emulsions can be stabilized for a longer time. However, in small-sized GO sheets, toluene droplets can be easily separated because the edge-to-surface ratio is high and the surfactant effect of smaller GO sheets is weak [26]. Compared to Pickering emulsions, an opposite amphiphilic nature is required in the case of the phase separation assembly of NGQDs at the liquid–liquid interface. Highly porous assemblies of hGO sheets can be fabricated by facile processing because the antisolvent effect of the extremely small-sized NGQDs is stronger than rGO nanosheets. In this paper, we define that appropriate size is critical for achieving an outstanding porous structure by the phase separation of NGQDs.

To better understand the aggregation mechanism and kinetics, we compared the optical properties of NGQD colloids before and after aggregation. Fig. 8(a) shows the absorbance of the GD-1 and GD-50 colloids before and after adding the DMA antisolvent (approximately 5%). It is interesting to note that the absorbance range of GD-1 increased for n-π* and surface state related transitions. In contrast, the aggregation of GD-50 favored the hypochromic shift in absorbance by promoting high-energy (π-π*) excitations [49,52]. The red and blue-shifted absorbance of GD-1 and GD-50 validate the J-type and H-type aggregation, even by the addition of a small amount of antisolvent [52]. The dipole–dipole interactions and hydrogen bonding between the antisolvent and GD-1 cause the head-to-tail assembly of the consecutive transition dipoles of GD-1, thereby forming J-aggregates [53]. In contrast, the deprotonation of GD-50 in the antisolvent facilitates the side-by-side assembly of the neighboring transition dipole, which is responsible for the stacked H-aggregates [54]. The aggregation mode has been reported to affect the Foster resonance energy transfer of electrons (FRET) and associated band structure [52]. Fig. 8(b) shows the variance in the bandgap caused by the aggregation of NGQDs. Compared to the bandgap of individual dispersed NGQDs, the J-type aggregation lowers the bandgap, as expected for GD-1. Conversely, H-type aggregates show a higher bandgap compared to individual quantum dots, as depicted for GD-50. For electrocatalytic activity, the lower bandgap of GD-1 is favorable as higher conductivity and electron transfer at lower potential is possible in lower-bandgap carbon materials [55]. This hypothesis is consistent with the low E_{PP} of the oriented GD-1@hGO composite structure. In conclusion, the aggregation-induced orientation of GD-1 not only provides a higher surface area but also modulates the electronic band structure to enhance the electrocatalytic activity.

Other parameters contributing to the superior electrocatalytic activity were evaluated through interface analysis of the composite structure [56,57]. Improved electrolyte and electrode interactions were evaluated using water contact angle, as shown in Fig. 8(c). The water contact angles of the rGO and composite electrode were 35° and 25°, respectively. The lower contact angles reflect the superior surface functionality of the composite electrode. Moreover, the stacked sheet structure of the rGO films and the porous and rough topology of the composite electrode are clearly observable in the AFM scan, shown in Fig. 8(d). Similarly, the composite electrode exhibited surface roughness that is four times higher than that of the rGO electrode. The higher surface roughness of oriented GD-1@hGO implies that a higher interface is available for the redox reaction. Apart from the higher surface roughness, the higher surface area of the optimized sample (BET surface area given in Table 1) is in agreement with the enhanced performance. From these tests, we can confirm that the superior electrocatalytic activity of the composite electrode can be attributed to its higher content of active sites, which are readily available for the catalytic reaction. With the proposed modification, a comparable efficiency to other recently reported counter electrodes was achieved (Table S1).

4. Conclusion

A highly porous 3D framework of hGO was achieved by utilizing a strong phase-separated assembly of GD-1 using DMA as an

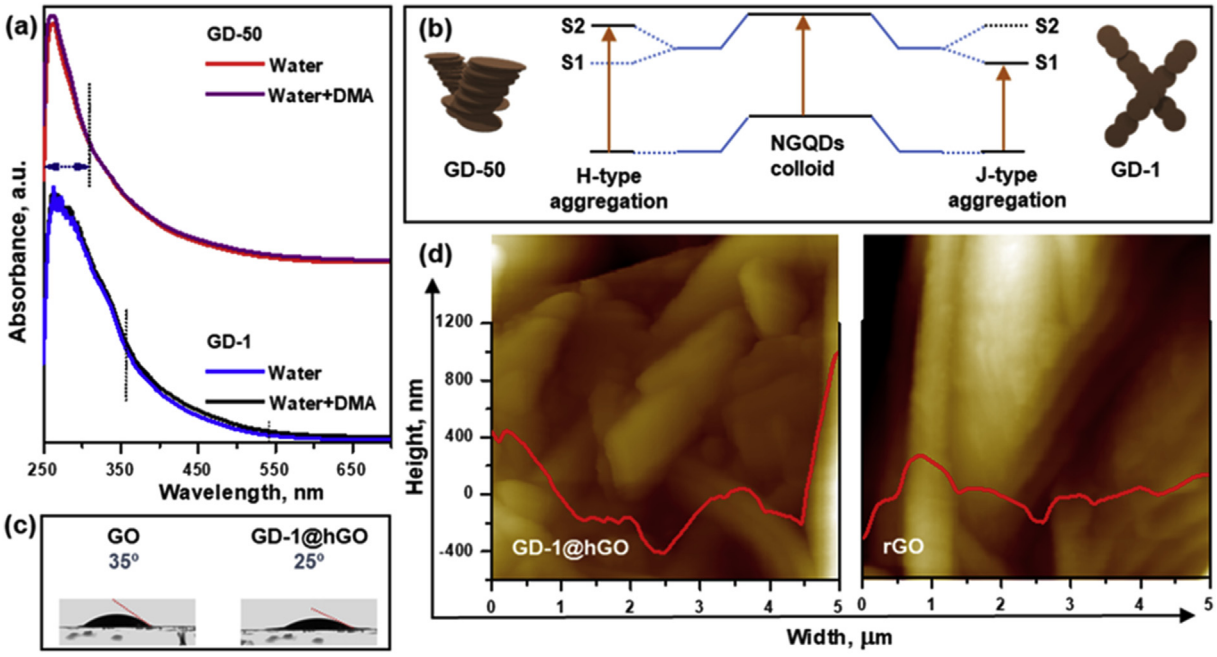

Fig. 8. (a) UV visible absorption spectrum of NGQDs after aggregation indicating their J or H type aggregation. (b) Variation in the band structure before and after aggregation of NGQDs. (c) Water contact angle of the composite and rGO electrode. (d) AFM images showing surface roughness of the electrodes. (A colour version of this figure can be viewed online.)

antisolvent. The antisolvent effect of GD-10 and GD-50 was negligible in the presence of hGO sheets; however, pure films of NGQDs exhibited intricate assemblies. The electrocatalytic performance of the assembled structure was three times higher than that of the stacked rGO structure. In addition, the charge transfer resistance was drastically reduced in the oriented hGO structure, which can be attributed to reduced radial electrolyte paths and multidimensional charge transport channels. The unobstructed channels for fast electrolyte diffusion and enhanced charge transfer interface drastically reduce the internal resistance of the solar cells. Hence, a DSSC fabricated with GD-1@hGO achieved significantly enhanced FF and associated power conversion efficiency. The superior electrocatalytic activity could be attributed to superior electrolyte interface, effective band structure tuning (by J-type aggregation and nitrogen doping), and excellent surface reactivity of the composite structure. Our proposed strategy of utilizing the lower-dimensional derivative of graphene to orient the 2D nanomaterials can be employed to boost the performance of next-generation electrochemical devices, such as supercapacitors, fuel cells, and batteries.

CRediT authorship contribution statement

Mumtaz Ali: Conceptualization, Methodology, Formal Analysis, Writing – Original Draft. **Rabia Riaz:** Conceptualization, Investigation. **Aima Sameen Anjum:** Investigation, Formal analysis, Validation. **Kyung Chul Sun:** Investigation, Resources, Writing – Review & Editing. **Li Hui:** Formal analysis, Resources. **Sung Hoon Jeong:** Supervision, Project administration. **Min Jae Ko:** Funding acquisition, Supervision.

Declaration of competing interest

The authors declare that they have no known competing financial interests or personal relationships that could have appeared to influence the work reported in this paper.

Acknowledgments

This work was supported by the Technology Development Program to Solve Climate Change (2017M1A2A2087353), and Research Program (2018R1A2B2006708) funded by the National Research Foundation under the Ministry of Science and ICT, Republic of Korea. This work is also supported by the Korea Institute of Energy Technology Evaluation and Planning (KETEP) and the Ministry of Trade, Industry and Energy (MOTIE) of the Republic of Korea (No. 20173010013200 and No. 2018201010636A). This work was supported by the National Research Foundation of Korea (NRF) grant funded by the Korea government (MIST) (No. 2019R1F1A1061267).

Appendix A. Supplementary data

Supplementary data to this article can be found online at https://doi.org/10.1016/j.carbon.2020.09.031.

References

[1] P. Chen, L. Wang, G. Wang, M. Gao, J. Ge, W. Yuan, Y. Shen, A. Xie, S. Yu, Nitrogen doped nanoporous carbon nanosheets derived from plant biomass: an efficient catalyst for oxygen reduction reaction, Energy Environ. Sci. 7 (2014) 4095–4103, https://doi.org/10.1039/c4ee02531h.

[2] J. Yang, H. Sun, H. Liang, H. Ji, L. Song, C. Gao, H. Xu, A highly effi cient metal-free oxygen reduction electrocatalyst assembled from carbon nanotubes and graphene, Adv. Mater. 28 (2016) 4606–4613, https://doi.org/10.1002/adma.201505855.

[3] J. Zhu, K. Li, M. Xiao, C. Liu, Z. Wu, J. Ge, W. Xing, Significantly enhanced oxygen reduction reaction performance of N-doped carbon by heterogeneous sulfur incorporation: synergistic effect between the two dopants in metal-free catalysts, J. Mater. Chem. A. 4 (2016) 7422–7429, https://doi.org/10.1039/c6ta02419j.

[4] H. Wang, X. Yuan, G. Zeng, Y. Wu, Y. Liu, Q. Jiang, S. Gu, Three dimensional graphene based materials: synthesis and applications from energy storage and conversion to electrochemical sensor and environmental remediation, Adv. Colloid Interface Sci. 221 (2015) 41–59, https://doi.org/10.1016/j.cis.2015.04.005.

[5] R. Wang, K.Q. Lu, F. Zhang, Z.R. Tang, Y.J. Xu, 3D carbon quantum dots/graphene aerogel as a metal-free catalyst for enhanced photosensitization efficiency, Appl. Catal. B Environ. 233 (2018) 11–18, https://doi.org/10.1016/j.apcatb.2018.03.108.

[6] R. Riaz, M. Ali, H. Anwer, M.J. Ko, S.H. Jeong, Highly porous self-assembly of nitrogen-doped graphene quantum dots over reduced graphene sheets for photo-electrocatalytic electrode, J. Colloid Interface Sci. 557 (2019) 174–184, https://doi.org/10.1016/j.jcis.2019.09.028.

[7] A.R. Raghavan, N. Alexander, Y. Liu, A general approach to multicomponent metal- decorated crumpled reduced graphene oxide nanocomposites using a fl ame-based process †, Nanoscale 11 (2019) 19571–19578, https://doi.org/10.1039/c9nr05792g.

[8] X. Chen, Y. Ren, T. Jiang, L. Hou, H. Jiang, High-throughput and multimodal separation of microbeads using cyclical induced-charge electro-osmotic vortices and its application in size fractionation of crumpled graphene oxide balls, Appl. Mater. Today. 19 (2020) 100545, https://doi.org/10.1016/j.apmt.2019.100545.

[9] J.Y. Kim, J.Y. Lee, K.Y. Shin, H. Jeong, H.J. Son, C.H. Lee, J.H. Park, S.S. Lee, J.G. Son, M.J. Ko, Highly crumpled graphene nano-networks as electrocatalytic counter electrode in photovoltaics, Appl. Catal. B Environ. 192 (2016) 342–349, https://doi.org/10.1016/j.apcatb.2016.04.008.

[10] R. Riaz, M. Ali, T. Maiyalagan, A.A. Arbab, A.S. Anjum, S. Lee, M.J. Ko, S.H. Jeong, Activated charcoal and reduced graphene sheets composite structure for highly electro-catalytically active counter electrode material and water treatment, Int. J. Hydrogen Energy 45 (2020) 7751–7763, https://doi.org/10.1016/j.ijhydene.2019.06.138.

[11] Z. Zhang, C.S. Lee, W. Zhang, Vertically aligned graphene nanosheet arrays: synthesis, properties and applications in electrochemical energy conversion and storage, Adv. Energy Mater. 1700678 (2017) 1–20, https://doi.org/10.1002/aenm.201700678.

[12] P. Du, K. Hu, J. Lyu, H. Li, X. Lin, G. Xie, X. Liu, Y. Ito, H. Qiu, Environmental Anchoring Mo single atoms/clusters and N on edge-rich nanoporous holey graphene as bifunctional air electrode in Zn – air batteries, Appl. Catal. B Environ. 276 (2020) 119172, https://doi.org/10.1016/j.apcatb.2020.119172.

[13] Y. Bian, H. Wang, J. Hu, B. Liu, D. Liu, L. Dai, Nitrogen-rich holey graphene for ef fi cient oxygen reduction reaction, Carbon N. Y. 162 (2020) 66–73, https://doi.org/10.1016/j.carbon.2020.01.110.

[14] K. Cao, H. Huang, F. Li, H. Yao, J. Bai, P. Chen, P. Jin, Z. Deng, J. Zeng, Y. Chen, Co nanoparticles supported on three-dimensionally N-doped holey graphene aerogels for electrocatalytic oxygen reduction, J. Colloid Interface Sci. 559 (2020) 143–151, https://doi.org/10.1016/j.jcis.2019.10.025.

[15] Y. Yan, J. Gong, J. Chen, Z. Zeng, W. Huang, K. Pu, J. Liu, P. Chen, Recent advances on graphene quantum Dots : from chemistry and physics to applications, Adv. Mater. 31 (2019) 1–22, https://doi.org/10.1002/adma.201808283.

[16] H. Park, S. Hyun Noh, J. Hye Lee, W. Jun Lee, J. Yun Jaung, S. Geol Lee, T. Hee Han, Large scale synthesis and light emitting fibers of tailor-made graphene quantum dots, Sci. Rep. 5 (2015) 1–9, https://doi.org/10.1038/srep14163.

[17] G. Xin, T. Yao, H. Sun, S.M. Scott, D. Shao, G. Wang, J. Lian, Highly thermally conductive and mechanically strong graphene fibers, Science 349 (80-) (2015) 1083–1088.

[18] K.H. Lee, H. Park, W. Eom, D.J. Kang, S.H. Noh, T.H. Han, Graphene quantum dots/graphene fiber nanochannels for osmotic power generation, J. Mater. Chem. A. 7 (2019) 23727–23732, https://doi.org/10.1039/c9ta05242a.

[19] L. Mao, H. Park, R.A. Soler-Crespo, H.D. Espinosa, T.H. Han, S.B.T. Nguyen, J. Huang, Stiffening of graphene oxide films by soft porous sheets, Nat. Commun. 10 (2019) 4–10, https://doi.org/10.1038/s41467-019-11609-8.

[20] M.J. Sweetman, S.M. Hickey, D.A. Brooks, J.D. Hayball, S.E. Plush, A practical guide to prepare and synthetically modify graphene quantum dots, Adv. Funct. Mater. 29 (2019) 1808740, https://doi.org/10.1002/adfm.201808740.

[21] R. Riaz, M. Ali, I.A. Sahito, A.A. Arbab, T. Maiyalagan, A.S. Anjum, M.J. Ko, S.H. Jeong, Self-assembled nitrogen-doped graphene quantum dots (N-GQDs) over graphene sheets for superb electro-photocatalytic activity, Appl. Surf. Sci. 480 (2019) 1035–1046, https://doi.org/10.1016/j.apsusc.2019.02.228.

[22] A.S. Sokolov, M. Ali, R. Riaz, Y. Abbas, M.J. Ko, C. Choi, Silver-adapted diffusive memristor based on organic nitrogen-doped graphene oxide quantum dots (N-GOQDs) for artificial biosynapse applications, Adv. Funct. Mater. 29 (2019) 1807504, https://doi.org/10.1002/adfm.201807504.

[23] K.C. Sun, A.A. Arbab, I.A. Sahito, M.B. Qadir, B.J. Choi, S.C. Kwon, S.Y. Yeo, S.C. Yi, S.H. Jeong, A PVdF-based electrolyte membrane for a carbon counter electrode in dye-sensitized solar cells, RSC Adv. 7 (2017) 20908–20918, https://doi.org/10.1039/c7ra00005g.

[24] K.C. Sun, I.A. Sahito, J.W. Noh, S.Y. Yeo, J.N. Im, S.C. Yi, Y.S. Kim, S.H. Jeong, Highly efficient and durable dye-sensitized solar cells based on a wet-laid PET membrane electrolyte, J. Mater. Chem. A. 4 (2016) 458–465, https://doi.org/10.1039/c5ta07720f.

[25] Y. Zheng, Y. Jiao, S.Z. Qiao, Engineering of carbon-based electrocatalysts for emerging energy conversion: from fundamentality to functionality, Adv.

Mater. 27 (2015) 5372–5378, https://doi.org/10.1002/adma.201500821.
[26] J. Kim, L.J. Cote, F. Kim, W. Yuan, K.R. Shull, J. Huang, Graphene oxide sheets at interfaces, J. Am. Chem. Soc. 132 (2010) 8180–8186, https://doi.org/10.1021/ja102777p.
[27] D. Qu, M. Zheng, L. Zhang, H. Zhao, Z. Xie, X. Jing, R.E. Haddad, H. Fan, Z. Sun, Formation mechanism and optimization of highly luminescent N-doped graphene quantum dots, Sci. Rep. 4 (2014) 5294–5305, https://doi.org/10.1038/srep05294.
[28] H. Ding, S.B. Yu, J.S. Wei, H.M. Xiong, Full-color light-emitting carbon dots with a surface-state-controlled luminescence mechanism, ACS Nano 10 (2016) 484–491, https://doi.org/10.1021/acsnano.5b05406.
[29] J. Peng, W. Gao, B.K. Gupta, Z. Liu, R. Romero-Aburto, L. Ge, L. Song, L.B. Alemany, X. Zhan, G. Gao, S.A. Vithayathil, B.A. Kaipparettu, A.A. Marti, T. Hayashi, J.J. Zhu, P.M. Ajayan, Graphene quantum dots derived from carbon fibers, Nano Lett. 12 (2012) 844–849, https://doi.org/10.1021/nl2038979.
[30] B. Bera, A. Chakraborty, T. Kar, P. Leuaa, M. Neergat, Density of states, carrier concentration, and flat band potential derived from electrochemical impedance measurements of N-doped carbon and their influence on electrocatalysis of oxygen reduction reaction, J. Phys. Chem. C 121 (2017) 20850–20856, https://doi.org/10.1021/acs.jpcc.7b06735.
[31] Y. Jiao, Y. Zheng, M. Jaroniec, S.Z. Qiao, Origin of the electrocatalytic oxygen reduction activity of graphene-based catalysts: a roadmap to achieve the best performance, J. Am. Chem. Soc. 136 (2014) 4394–4403, https://doi.org/10.1021/ja500432h.
[32] M. Ali, R. Riaz, S. Bae, H.S. Lee, S.H. Jeong, M.J. Ko, Layer-by-Layer self-assembly of hollow nitrogen-doped carbon quantum dots on cationized textured crystalline silicon solar cells for an efficient energy down-shift, ACS Appl. Mater. Interfaces 12 (2020) 10369–10381, https://doi.org/10.1021/acsami.9b21087.
[33] F. Mateen, M. Ali, H. Oh, S.-K. Hong, Nitrogen-doped carbon quantum dot based luminescent solar concentrator coupled with polymer dispersed liquid crystal device for smart management of solar spectrum, Sol. Energy 178 (2019) 48–55, https://doi.org/10.1016/j.solener.2018.12.013.
[34] F. Mateen, M. Ali, S.Y. Lee, S.H. Jeong, M.J. Ko, S.K. Hong, Tandem structured luminescent solar concentrator based on inorganic carbon quantum dots and organic dyes, Sol. Energy 190 (2019) 488–494, https://doi.org/10.1016/j.solener.2019.08.045.
[35] A. Sharma, T. Gadly, A. Gupta, A. Ballal, S.K. Ghosh, M. Kumbhakar, Origin of excitation dependent fluorescence in carbon nanodots, J. Phys. Chem. Lett. 7 (2016) 3695–3702, https://doi.org/10.1021/acs.jpclett.6b01791.
[36] S. Zhu, Y. Song, X. Zhao, J. Shao, J. Zhang, B. Yang, The photoluminescence mechanism in carbon dots (graphene quantum dots, carbon nanodots, and polymer dots): current state and future perspective, Nano Res 8 (2015) 355–381, https://doi.org/10.1007/s12274-014-0644-3.
[37] J. Ma, C. Li, F. Yu, J. Chen, "Brick-like" N-doped graphene/carbon nanotube structure forming three-dimensional films as high performance metal-free counter electrodes in dye-sensitized solar cells, J. Power Sources 273 (2015) 1048–1055, https://doi.org/10.1016/j.jpowsour.2014.10.003.
[38] D.W. Zhang, X.D. Li, H.B. Li, S. Chen, Z. Sun, X.J. Yin, S.M. Huang, Graphene-based counter electrode for dye-sensitized solar cells, Carbon N. Y. 49 (2011) 5382–5388, https://doi.org/10.1016/j.carbon.2011.08.005.
[39] D.R. Paul, W.J. Koros, R.Y.F. Liu, Y.S. Hu, E. Baer, A. Hiltner, H.D. Keith, R.Y.F. Liu, A. Hiltner, E. Baer, R.E. Cohen, A. Bellare, R.J. Albalak, W. Hu, G. Reiter, Nitrogen-doped carbon nanotube arrays with high electrocatlytic activity for oxygen reduction, Science 323 (80-) (2009) 760–763.
[40] Q. Li, S. Zhang, L. Dai, L.S. Li, Nitrogen-doped colloidal graphene quantum dots and their size-dependent electrocatalytic activity for the oxygen reduction reaction, J. Am. Chem. Soc. 134 (2012) 18932–18935, https://doi.org/10.1021/ja309270h.
[41] J. Zhang, Z. Zhao, Z. Xia, L. Dai, A metal-free bifunctional electrocatalyst for oxygen reduction and oxygen evolution reactions, Nat. Nanotechnol. 10 (2015) 444–452, https://doi.org/10.1038/nnano.2015.48.
[42] J. Wu, Z. Pan, Y. Zhang, B. Wang, H. Peng, The recent progress of nitrogen-doped carbon nanomaterials for electrochemical batteries, J. Mater. Chem. A. 6 (2018) 12932–12944, https://doi.org/10.1039/c8ta03968b.
[43] Z. Pan, J. Ren, G. Guan, X. Fang, B. Wang, S.G. Doo, I.H. Son, X. Huang, H. Peng, Synthesizing nitrogen-doped core–sheath carbon nanotube films for flexible lithium ion batteries, Adv. Energy Mater. 6 (2016) 1–6, https://doi.org/10.1002/aenm.201600271.
[44] A. Eftekhari, The mechanism of ultrafast supercapacitors, J. Mater. Chem. A. 6 (2018) 2866–2876, https://doi.org/10.1039/c7ta10013b.
[45] J.D. Roy-Mayhew, D.J. Bozym, C. Punckt, I.A. Aksay, Functionalized graphene as a catalytic counter electrode in dye-sensitized solar cells, ACS Nano 4 (2010) 6203–6211, https://doi.org/10.1021/nn1016428.
[46] S. Zhang, N. Pan, Supercapacitors performance evaluation, Adv. Energy Mater. 5 (2015) 1–19, https://doi.org/10.1002/aenm.201401401.
[47] W.H. Shin, H.M. Jeong, B.G. Kim, J.K. Kang, J.W. Choi, Nitrogen-doped multiwall carbon nanotubes for lithium storage with extremely high capacity, Nano Lett. 12 (2012) 2283–2288, https://doi.org/10.1021/nl3000908.
[48] J. Gao, X. Song, X. Huang, L. Wang, B. Li, H. Xue, Facile preparation of polymer microspheres and fibers with a hollow core and porous shell for oil adsorption and oil/water separation, Appl. Surf. Sci. 439 (2018) 394–404, https://doi.org/10.1016/j.apsusc.2018.01.013.
[49] J.S. Anjali Devi, R.S. Aparna, R.R. Anjana, J. Nebu, S.M. Anju, S. George, Solvent effects: a signature of J- and H-aggregate of carbon nanodots in polar solvents, J. Phys. Chem. 123 (2019) 7420–7429, https://doi.org/10.1021/acs.jpca.9b04568.
[50] S.H. Lee, H.W. Kim, J.O. Hwang, W.J. Lee, J. Kwon, C.W. Bielawski, R.S. Ruoff, S.O. Kim, Three-dimensional self-assembly of graphene oxide platelets into mechanically flexible macroporous carbon films, Angew. Chem. Int. Ed. 49 (2010) 10084–10088, https://doi.org/10.1002/anie.201006240.
[51] S. Yin, Y. Zhang, J. Kong, C. Zou, C.M. Li, X. Lu, J. Ma, F.Y.C. Boey, X. Chen, Assembly of graphene sheets into hierarchical structures for high-performance energy storage, ACS Nano 5 (2011) 3831–3838, https://doi.org/10.1021/nn2001728.
[52] N.J. Hestand, F.C. Spano, Expanded theory of H- and J-molecular aggregates: the effects of vibronic coupling and intermolecular charge transfer, Chem. Rev. 118 (2018) 7069–7163, https://doi.org/10.1021/acs.chemrev.7b00581.
[53] H. Qian, M.E. Cousins, E.H. Horak, A. Wakefield, M.D. Liptak, I. Aprahamian, Suppression of Kasha's rule as a mechanism for fluorescent molecular rotors and aggregation-induced emission, Nat. Chem. 9 (2017) 83–87, https://doi.org/10.1038/nchem.2612.
[54] A.P. Demchenko, V.I. Tomin, P.T. Chou, Breaking the kasha rule for more efficient photochemistry, Chem. Rev. 117 (2017) 13353–13381, https://doi.org/10.1021/acs.chemrev.7b00110.
[55] Q. Li, S. Zhang, L. Dai, L. Li, Nitrogen-doped colloidal graphene quantum dots and their size-dependent electrocatalytic activity for the oxygen reduction reaction, J. Am. Chem. Soc. 134 (2012) 18932–18935, https://doi.org/10.1021/ja309270h.
[56] J. Zou, B. Wang, B. Zhu, Y. Yang, W. Han, A. Dong, Fe, N, S-codoped carbon frameworks derived from nanocrystal superlattices towards enhanced oxygen reduction activity, Nano Converg. 6 (2019), https://doi.org/10.1186/s40580-019-0174-5.
[57] J. John, D.K. Lee, U. Sim, Photocatalytic and electrocatalytic approaches towards atmospheric nitrogen reduction to ammonia under ambient conditions, Nano Converg. 6 (2019), https://doi.org/10.1186/s40580-019-0182-5.